Probing for high-momentum protons in ^{4}He via the ^{4}He$(e, e'p)X$ reactions

S. Iqbal,[1] F. Benmokhtar,[2,*] M. Ivanov,[3] N. See,[1] K. Aniol,[1] D. W. Higinbotham,[4] C. Boyd,[2] A. Gadsby,[2] J. S. Goodwill,[2] D. Finton,[2] A. Boyer,[2] S. Gilad,[5] A. Saha,[4,†] J. M. Udias,[6] Z. Ye,[7] P. Solvignon,[4,†] P. Aguilera,[8] Z. Ahmed,[9] H. Albataineh,[10] K. Allada,[4] B. Anderson,[11] D. Anez,[12] J. Annand,[13] J. Arrington,[14] T. Averett,[15] H. Baghdasaryan,[16] X. Bai,[17] A. Beck,[18] S. Beck,[18] V. Bellini,[19] A. Camsonne,[4] C. Chen,[20] J.-P. Chen,[4] K. Chirapatpimol,[16] E. Cisbani,[21] M. M. Dalton,[16,4] A. Daniel,[22] D. Day,[16] W. Deconinck,[5] M. Defurne,[23] D. Flay,[24] N. Fomin,[25] M. Friend,[26] S. Frullani,[21] E. Fuchey,[24] F. Garibaldi,[21] D. Gaskell,[4] R. Gilman,[27] S. Glamazdin,[28] C. Gu,[16] P. Guèye,[20] C. Hanretty,[16] J.-O. Hansen,[4] M. Hashemi Shabestari,[16] M. Huang,[29] G. Jin,[16] N. Kalantarians,[30] H. Kang,[31] A. Kelleher,[5] I. Korover,[32] J. LeRose,[4] J. Leckey,[33] R. Lindgren,[16] E. Long,[11] J. Mammei,[34] D. J. Margaziotis,[1] P. Markowitz,[35] D. Meekins,[4] Z. Meziani,[24] R. Michaels,[4] M. Mihovilovic,[36] N. Muangma,[5] C. Munoz Camacho,[37] B. Norum,[16] Nuruzzaman,[38] K. Pan,[5] S. Phillips,[39] E. Piasetzky,[32] I. Pomerantz,[32] M. Posik,[24] V. Punjabi,[40] X. Qian,[29] Y. Qiang,[4] X. Qiu,[41] P. E. Reimer,[7] A. Rakhman,[9] S. Riordan,[16,42] G. Ron,[43] O. Rondon-Aramayo,[16,4] L. Selvy,[11] A. Shahinyan,[44] R. Shneor,[32] S. Sirca,[45,36] K. Slifer,[39] N. Sparveris,[24] R. Subedi,[16] V. Sulkosky,[5] D. Wang,[16] J. W. Watson,[11] L. B. Weinstein,[46] B. Wojtsekhowski,[4] S. A. Wood,[4] I. Yaron,[32] X. Zhan,[7] J. Zhang,[4] Y. W. Zhang,[27] B. Zhao,[15] X. Zheng,[16] P. Zhu,[47] and R. Zielinski[39]

(Jefferson Lab Hall A Collaboration)

[1]*California State University, Los Angeles, Los Angeles, California 90032, USA*

[2]*Duquesne University, Pittsburgh, Pennsylvania 15282, USA*

[3]*Bulgarian Academy of Sciences, Sofia, Bulgaria*

[4]*Thomas Jefferson National Accelerator Facility, Newport News, Virginia 23606, USA*

[5]*Massachusetts Institute of Technology, Cambridge, Massachusetts 02139, USA*

[6]*Computense University de Madrid, Madrid, Spain*

[7]*Physics Division, Argonne National Laboratory, Lemont, Illinois 60439, USA*

[8]*Institut de Physique Nucléaire (UMR 8608), CNRS/IN2P3-Université Paris-Sud, F-91406 Orsay Cedex, France*

[9]*Syracuse University, Syracuse, New York 13244, USA*

[10]*Texas A&M University, Kingsville, Texas 78363, USA*

[11]*Kent State University, Kent, Ohio 44242, USA*

[12]*Saint Mary's University, Halifax, Nova Scotia, Canada*

[13]*University of Glasgow, Glasgow G12 8QQ, Scotland, United Kingdom*

[14]*Lawrence Berkeley National Laboratory, Berkeley, California 94720, USA*

[15]*College of William and Mary, Williamsburg, Virginia 23187, USA*

[16]*University of Virginia, Charlottesville, Virginia 22904, USA*

[17]*China Institute of Atomic Energy, Beijing, China*

[18]*Nuclear Research Center Negev, Beer-Sheva, Israel*

[19]*Universita di Catania, Catania, Italy*

[20]*Hampton University, Hampton, Virginia 23668, USA*

[21]*INFN, Sezione Sanità and Istituto Superiore di Sanità, 00161 Rome, Italy*

[22]*Ohio University, Athens, Ohio 45701, USA*

[23]*CEA Saclay, F-91191 Gif-sur-Yvette, France*

[24]*Temple University, Philadelphia, Pennsylvania 19122, USA*

[25]*University of Tennessee, Knoxville, Tennessee 37996, USA*

[26]*Carnegie Mellon University, Pittsburgh, Pennsylvania 15213, USA*

[27]*Rutgers, The State University of New Jersey, Piscataway, New Jersey 08855, USA*

[28]*Kharkov Institute of Physics and Technology, Kharkov 61108, Ukraine*

[29]*Duke University, Durham, North Carolina 27708, USA*

[30]*Virginia Union University, Richmond, Virginia 23220, USA*

[31]*Seoul National University, Seoul, Korea*

[32]*Tel Aviv University, Tel Aviv 69978, Israel*

[33]*Indiana University, Bloomington, Indiana 47405, USA*

[34]*Virginia Polytechnic Institute and State University, Blacksburg, Virginia 24061, USA*

[35]*Florida International University, Miami, Florida 33199, USA*

[36]*Jozef Stefan Institute, Ljubljana, Slovenia*

[*]Corresponding author: benmokhtarf@duq.edu

[†]Deceased.

[37]*Université Blaise Pascal/IN2P3, F-63177 Aubière, France*
[38]*Mississippi State University, Mississippi State, Mississippi 39762, USA*
[39]*University of New Hampshire, Durham, New Hampshire 03824, USA*
[40]*Norfolk State University, Norfolk, Virgina 23504, USA*
[41]*Lanzhou University, Lanzhou, China*
[42]*University of Massachusetts, Amherst, Massachusetts 01006, USA*
[43]*Racah Institute of Physics, Hebrew University of Jerusalem, Jerusalem, Israel*
[44]*Yerevan Physics Institute, Yerevan 375036, Armenia*
[45]*Faculty of Mathematics and Physics, University of Ljubljana, Ljubljana, Slovenia*
[46]*Old Dominion University, Norfolk, Virginia 23529, USA*
[47]*University of Science and Technology, Hefei, China*

(Received 11 May 2019; revised 13 March 2022; accepted 14 April 2022; published 22 June 2022)

Experimental cross sections for the ^{4}He$(e, e'p)X$ reactions in the missing energy range from 0.017 to 0.022 GeV and up to a missing momentum of 0.632 GeV/c at $x_B = 1.24$ and $Q^2 = 2$ (GeV/c)^2 are reported. The data are compared to relativistic distorted-wave impulse approximation calculations for the ^{4}He$(e, e'p)^3$H channel. Significantly more events are observed for $p_m \geqslant 0.45$ GeV/c than are predicted by the theoretical model, and striking fluctuations in the ratio of data to the theoretical model around $p_m = 0.3$ GeV/c are possible signals of initial-state multinucleon correlations.

DOI: 10.1103/PhysRevC.105.064003

I. INTRODUCTION

Nucleon momentum distributions in atomic nuclei are known to be governed by an average nuclear potential plus additional nucleon-nucleon and nucleon-multibody interactions [1,2]. Momentum distributions below the Fermi momentum essentially reflect the size of the "box" in which the nucleons are contained. One way to model this distribution is in the simplest limit of a cluster model where a given nucleon interacts with the average potential of the other nucleons. For momenta greater than the Fermi momentum, the cluster models of nuclear structure provide enhanced strength in the momentum distribution to account for contributions with spatial distributions smaller than the average nucleon-nucleon spacing.

Cross sections are critical observables to test *ab initio* calculations of nucleon momentum distributions. The large numbers of nucleon-nucleon scattering data sets [3,4], based on neutron-proton or proton-proton reactions, are insufficient to account for the details of nucleon momentum distributions inferred from (e, e') inclusive electron scattering reactions, such as the proton-proton correlation function needed for the Coulomb sum rule [5]. In addition, two nucleon interactions alone cannot quantitatively explain the binding energies of low-mass nuclei [3,4]. Short-range correlations between two nucleons and three-body nucleon interactions are proposed to explain these observables. ^{4}He is the best nucleus to test theoretical nucleon momentum distributions because only four nucleons are involved in this many-body problem and its central density is close to that of larger nuclei.

Microscopic nuclear structure calculations based on realistic two- and three-body nucleon-nucleon calculations are available for low-mass nuclei [6]. In the case of ^{4}He, proton momentum distributions have been calculated for proton-triton (pt) and deuteron-deuteron (dd) clusters. Recent measurements of proton-nucleon coincidences in the ^{4}He$(e, e'pN)$ reaction [7–10] have shown strong correlations of back-to-back emission of nucleon pairs for large missing momentum $p_m > 400$ MeV/c. Moreover, the increase of the $\frac{\#pp}{\#pn}$ pair ratio as p_m increases above 400 MeV/c is interpreted as a sign that the nucleon-nucleon interaction is evolving from the tensor interaction to the strong repulsive short-range interaction.

Experimental access to proton momentum distributions in nuclei is possible through measurements of the differential cross section of the $A(e, e'p)X$ reaction and its dependence on the missing momentum p_m and the missing energy E_m. The $A(e, e'p)X$ reaction is illustrated in Fig. 1, where $\vec{p}_X = \vec{p}_e - \vec{p}_{e'} - \vec{p}_p$, and $p_m = |\vec{p}_X|$ is the momentum of the unmeasured particle(s) X [1]. The missing energy E_m of the reaction is the difference between the electron transferred energy ($\omega = E_e - E_{e'}$) and the kinetic energies of the knocked-out proton and system X, T_p and T_X, respectively: $E_m = \omega - T_p - T_X$. The energy of the incident electron is obtained from dedicated beam energy measurements, while the energies of the scattered electron and the knocked-out proton are deduced directly from their momenta, which are obtained from their respective spectrometer optics reconstruction. The total energy of system X is obtained by the conservation of the energy in the reaction. Knowing the momentum and the total energy of X, its mass can be obtained; therefore, its kinetic energy can be obtained.

Previous $(e, e'p)$ experiments were performed on different types of targets and as examples we cite here Refs. [11,12] on ^{3}He, Ref. [13] on deuteron, and Ref. [14] on ^{16}O.

Differential cross sections of proton knockout from ^{4}He have a history that started with electron beam energies below 1 GeV, as in Ref. [5]. But the low electron beam energy, 560 MeV, and small duty factor (1%) in that experiment

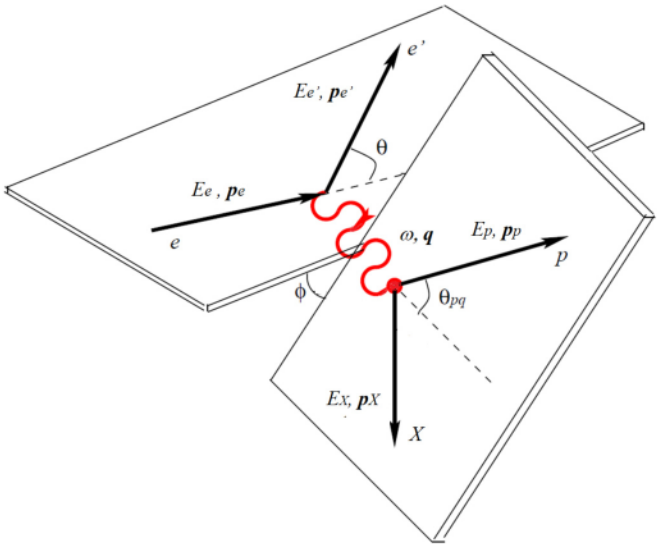

FIG. 1. Kinematic definitions for the $A(e, e'p)X$ reaction.

limited the data to small $x_B \ll 1$ and missing momenta between 225 and 600 MeV/c. This paper provides experimental differential cross sections in the missing energy region from 0.017 to 0.022 GeV, called the "triton" region, based on the ^{4}He$(e, e'p)X$ reaction over a range of missing momenta, $25 < p_m < 632$ MeV/c, and $x_B = 1.24$, where $X = {}^3$H, ^{2}H $+ n$, and $p + n + n$, in this paper collectively called the three-nucleon ($3N$) mass region. The data were taken during the E08009 experiment in Hall A at Jefferson Laboratory. These experimental results are compared to the state-of-the-art relativistic distorted-wave impulse approximation (RDWIA) calculations of the Madrid group [15] for the case $X = {}^3$H. However, spectra of missing energy at $p_m \geqslant 0.45$ GeV/c show incursions of the $X = {}^2$H $+ n$ and $p + n + n$ reactions into the "triton" region. There are no theoretical calculations available for these other final $3N$ states.

The rest of this paper is divided as follows. In Sec. II, the E08009 experimental setup is presented, explaining the spectrometer settings and the cryogenic target. The data analysis section is presented in Sec. III, covering background subtractions, coincidence events selection, momentum acceptance efficiency, straggling, and external bremsstrahlung. Details around the extraction of the cross section are presented in this section as well. In Sec. IV cross-section results are presented, where data are compared to the Madrid group's theoretical predictions. A discussion and conclusions are presented in Sec. V. Tables of experimental results and theoretical calculations are summarized in the Appendix.

II. EXPERIMENTAL SETUP

A. Spectrometer settings

Experiment E08009 [16] at the Thomas Jefferson National Accelerator Facility in experimental Hall A [17], ran in February, March, and April of 2011, in parallel with the triple coincidence short-range correlation experiment described in Ref. [7]. Data for kinematic settings of 0.153 and 0.353 GeV/c missing momentum were obtained using electron beam currents between 47 to 60 μA, for E08009. In addition to these kinematic settings the short-range correlation (SRC) [7] experiment also obtained data at kinematic settings out to 0.632 GeV/c missing momentum, including the multibody breakup channel $p + X$. These higher missing momenta data were collected using 4- to 5-μA electron beam currents but sufficient accumulated charge was measured to be able to extract cross sections beyond the original goal set for E08009. Moreover, the acceptances of the Hall A spectrometers allowed for cross sections to be determined across a larger missing momentum range than the central value kinematic settings would suggest.

TABLE I. Proton spectrometer settings.

Central p_m (GeV/c)	θ_p (deg.)	θ_{pq} (deg.)	Central momentum (GeV/c)
0.153	47.0	−2.4	1.500
0.353	38.5	−10.9	1.449
0.466	33.5	−15.9	1.383
0.632	29.0	−20.4	1.308

The electron spectrometer was fixed in angle and central momentum while the proton spectrometer's angles and central momenta were changed. The incident beam energy was 4.4506 GeV, the electron arm kinematic settings were as follows: electron spectrometer angle, 20.3°; electron spectrometer momentum, 3.602 GeV/c; four-momentum transfer, $Q^2 = 2.0$ (GeV/c)^2; Bjorken $x_b = 1.24$; and three-momentum transfer of 1.647 GeV/c at an angle $\theta_q = 49.4°$ with respect to the incident electron momentum. The proton arm settings are given in Table I.

B. Cryogenic target

The cryogenic target was gas ^{4}He contained in an aluminum can of a length of 20 cm. The nominal temperature of the gas was 20 K at 199 psi (absolute). ^{4}He entered and exited at the upstream end of the target. There was no outlet for the fluid at the downstream end of the can. A determination of target density along the beam path was done by comparing the normalized yield of scattered electrons at 47- and 60-μA beam currents to the yield at 4 μA. Since the electron spectrometer was held at a fixed momentum and angle, the electron spectrometer served as a density monitor. For this target at a beam current of 4 μA a computational fluid dynamics (CFD) calculation [18] predicts an average density drop of 2.3% from strictly thermodynamic parameters. A comparison of the measured yield at 4 μA to the CFD calculation gives an uncertainty in the target density dependence along the beam of 1.1%. More detail for the treatment of the target density used in the data analysis is available in Ref. [19]. Across the ±8 cm effective target length and for the different beam currents, the target densities are summarized in Table II.

TABLE II. Target density dependence on beam heating as a function of beam current.

Beam current (μA)	Target density (nuclei/cm^2)
4.014	$7.84 \pm 0.087 \times 10^{22}$
45.46	$6.732 \pm 0.077 \times 10^{22}$
60.71	$5.662 \pm 0.065 \times 10^{22}$

III. DATA ANALYSIS

A. Background subtraction and coincidence event selection

For this experiment, event triggers were generated by coincident signals from scintillator arrays. Particle tracks were reconstructed using the high-resolution spectrometer's vertical drift chambers. The small π^- background in the electron arm was rejected using a CO_2 gas Cherenkov detector. In the proton spectrometer, coincident π^+, and other positively charged nuclei like ^{2}H and ^{3}H were separated from the protons using the time difference between particles detected in the two spectrometers. Most of the accidental coincident events were rejected by cuts on the difference between interaction points in the target along the beam as reconstructed by the two spectrometers. The remaining accidental background was subtracted using the coincidence timing between the spectrometers. Figure 2 shows a coincidence time of flight for the 353 MeV/c kinematics. The number of real coincidence events in a 20-ns time window around the peak was obtained by subtracting the accidentals under the peak considering a flat background under the whole spectrum, as shown in Fig. 2.

The wide momentum acceptance of the spectrometers allows for a broad missing momentum acceptance as shown in Fig. 3, so we were able to divide the study in 50 MeV/c

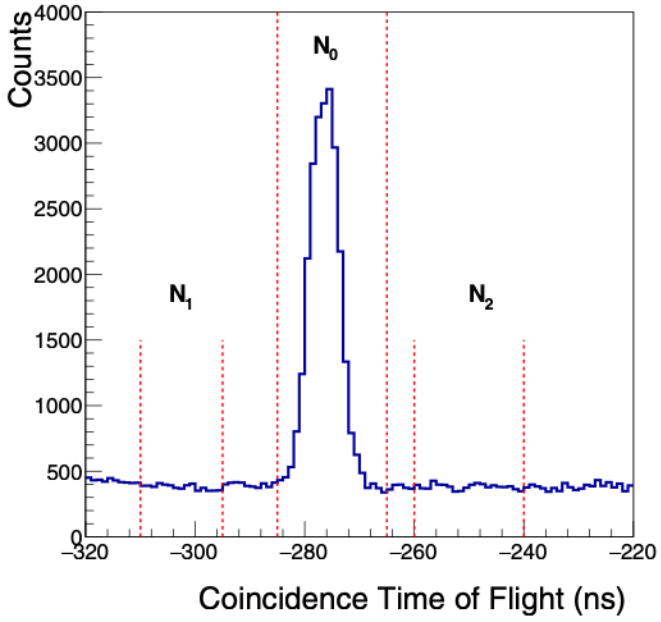

FIG. 2. Coincidence time-of-flight spectrum for the 353 MeV/c setting.

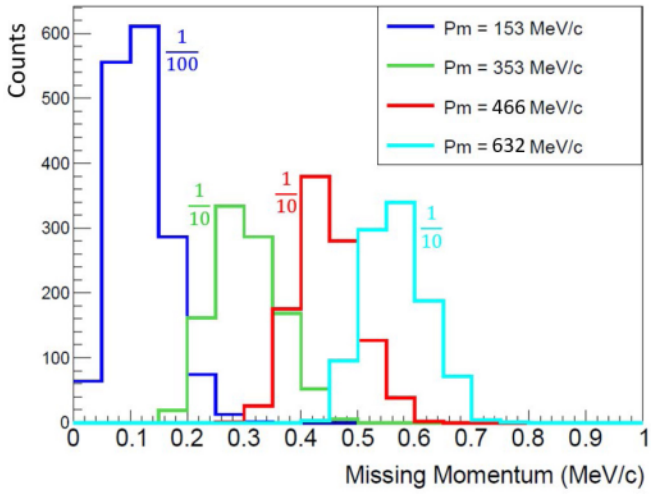

FIG. 3. Missing momentum spectra for all the kinematical settings of the experiment.

wide bins in p_m. For each kinematical bin, the number of true coincidence events N_t was determined from the coincidence time of flight with the following formula:

$$N_t = N_0 - \frac{\Delta t_0 (N_1 + N_2)}{\Delta t_1 + \Delta t_2}, \tag{1}$$

where N_0 is the number of events within the bin reconstructing in the real coincidence window Δt_0, and N_1 and N_2 are the number of events within the bin reconstructing in the accidental coincidence windows Δt_1 and Δ_{t_2}, respectively. Statistical uncertainties were propagated as

$$\delta N_t = \sqrt{N_r + (N_1 + N_2)} \left(\frac{\Delta t_0}{\Delta t_1} + \Delta t_2 \right)^2. \tag{2}$$

For the determination of the cross section, the following phase-space cuts were applied to the data for both electron and proton spectrometers: horizontal angle, ± 0.04 rad; vertical angle, ± 0.03 rad; vertex position, ± 8 cm; and the deviation from central momentum, $\pm 4.5\%$. These variables are shown in Fig. 4.

Missing energy spectra for all the kinematics after accidental and background subtraction are presented in Fig. 5. Figure 6 represents two-dimensional missing momentum versus missing energy spectra for the full data set. Note that the strength of the two-body cluster weakens while going from lower to higher momenta.

Data analysis was aided by the Monte Carlo simulation (GEANT 3.2 [20]) of the transport of the incident electron, the scattered electron, and the proton through the target cell into the spectrometer apertures, assuming a p + triton final hadronic state. The identification of the p + triton final state is possible by calculating the missing energy in the scattered electron + p state. A peak in the missing energy spectrum, at 19.8 MeV, corresponding to the triton ground state identifies the ^{4}He$(e, e'p)^3$H reaction, as seen in Fig. 5.

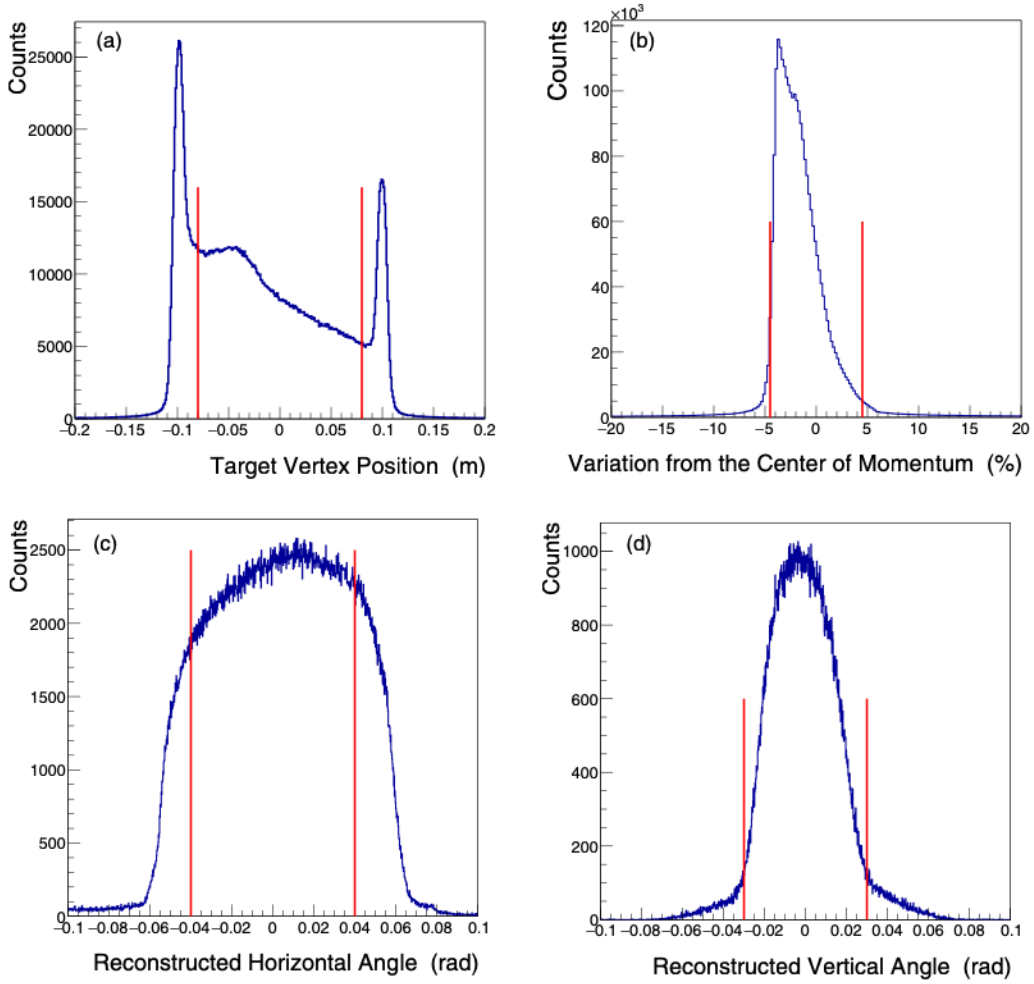

FIG. 4. (a) Target vertex position in meters. (b) Variation from the central momentum (%). (c) Reconstructed horizontal angle in radians. (d) Reconstructed vertical angle in radians.

B. Missing momentum acceptance efficiency

In the simulation a vertex point is chosen at random in the long gas target, which gives the incoming electron's momentum at the interaction point. Then hit points within the apertures of the spectrometers for the outgoing electron and proton are randomly selected. Each point within the spectrometers' apertures has an equal probability of being selected. This allows for the vertex angles of the electron and the proton to be determined. An energy for the outgoing electron is chosen within the momentum acceptance of the electron spectrometer. From the incident electron's momentum, the scattered electron's momentum, and the angles for the ejected proton, the three-body kinematics for the ^{4}He$(e, e'p)^3$H reaction allows for the proton's vertex momentum to be determined. The electron and the proton are followed from the vertex to the final hit points in the spectrometers' apertures. Thus, complete information about the location and momenta at the vertex and the spectrometers' apertures is known.

The three-body kinematical and geometrical limitations for particles arriving at the hit points within the apertures are calculated by GEANT and thus allow the missing momentum $\vec{p}_m = \vec{p}_e - \vec{p}_{e'} - \vec{p}_p$ to be calculated. In the analysis, we bin $|\vec{p}_m|$ into 50 MeV/c bins and we define the missing momentum acceptance factor $f(p_m)$ for a bin as

$$f(p_m) = \frac{n(p_m)}{\sum n(p_m)}. \tag{3}$$

where $n(p_m)$ is the number of triton events in the missing momentum bin centered on p_m and $\sum n(p_m)$ is the total number of triton events over all missing momenta for the particular proton kinematic setting. The same Gaussian broadening used for the simulation fit in Fig. 5(b) is used to generate the values of p_m needed to calculate $f(p_m)$.

The momentum resolution measured by the spectrometers in this experiment is a factor of 3 to 4 times larger than for a point target due to the 16 cm of target length we used. This shows up in the width of the missing energy spectra. We see from Fig. 5(b) a strong peak near the triton ground state and the background from other processes. When we compare our data to theory we are restricted to a window around the peak. However, the theoretical calculations usually do not include the scattering and radiative effects seen in the data.

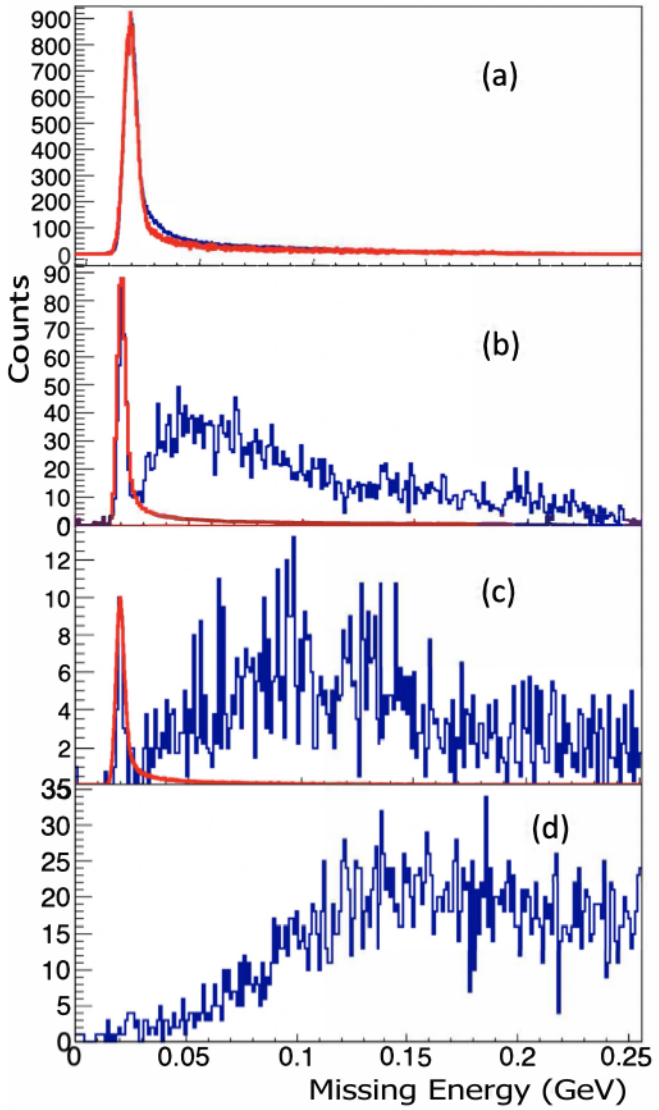

FIG. 5. Missing energy spectra for all the kinematical settings. Data are in blue and the simulated two-body breakup channel is in red. (a) $p_m = 153$ MeV/c, (b) $p_m = 353$ MeV/c, (c) $p_m = 466$ MeV/c, and (d) $p_m = 632$ MeV/c.

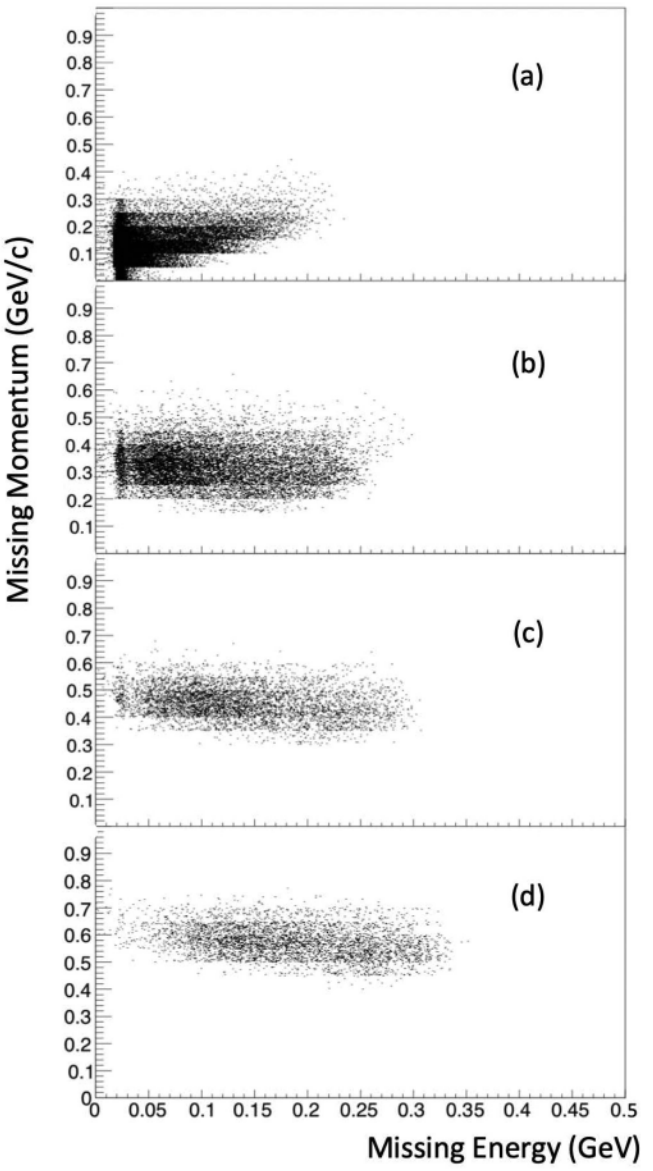

FIG. 6. Two-dimensional plots of missing momentum versus missing energy for the kinematical settings of the experiment. (a) $p_m = 153$ MeV/c, (b) $p_m = 353$ MeV/c, (c) $p_m = 466$ MeV/c, and (d) $p_m = 632$ MeV/c.

The missing momentum factor is our estimate of how many of the theoretical events fall outside our experimental window. There is a systematic uncertainty in this factor because it is only calculated by GEANT. Ideally, we want to use an independent experimentally determined missing momentum factor established on a well-known data set of (e, p) coincidences. However, such an experimental data set is not available over the full range of electron and proton momenta measured in this experiment. We were encouraged to see that this simple choice of missing momentum factor follows the theoretical predictions quite well (see Figs. 9 and 11). While this does not give a precise calibration of the acceptance, we estimate that the systematic uncertainty in $f(p_m)$ is 10%, which is conservative given the typical uncertainty in the acceptance when physics checks can be performed.

C. Peak-broadening effects

Straggling and external bremsstrahlung obtained from the GEANT simulation produce a broadening and a characteristic tail on the missing energy spectrum. In practice the long target introduces additional broadening beyond the intrinsic point source resolution of the spectrometers. The additional broadening is included in the simulation by a Gaussian smearing of the momenta at the apertures. It is typically a factor of 3 to 4 bigger than the resolution of the point source peak. The amount of Gaussian smearing needed is determined by the best fit of a strong missing energy data peak such as at the lowest missing momentum. An example of the fit is seen

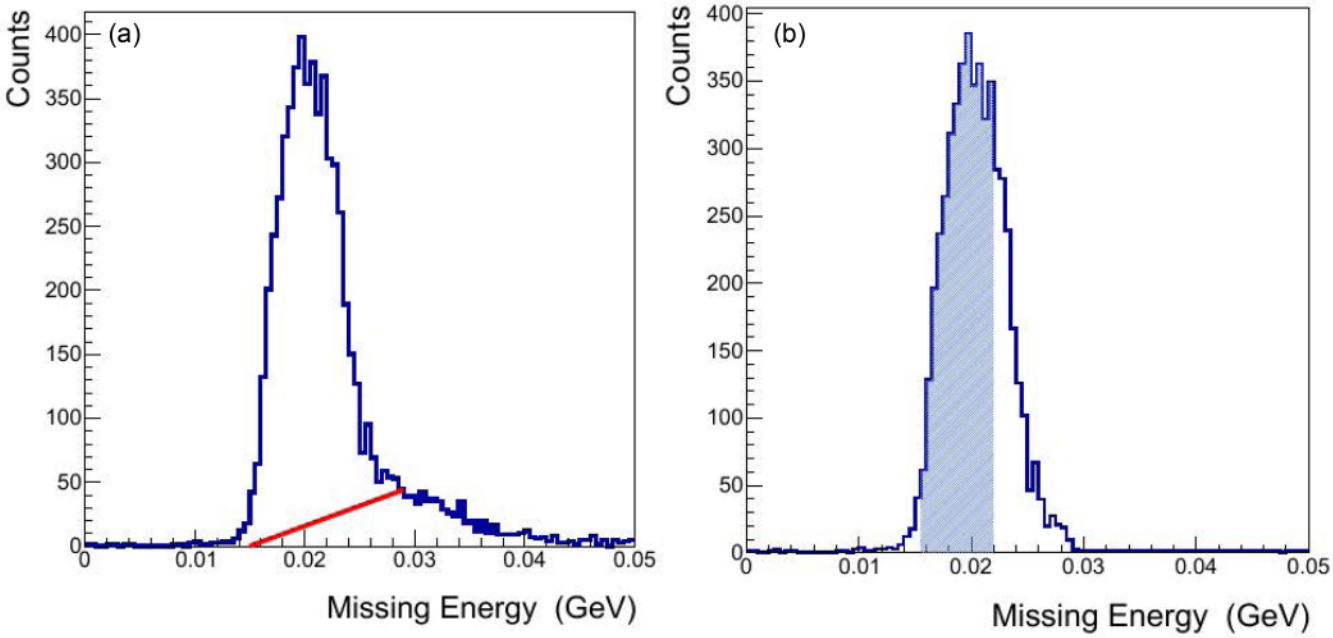

FIG. 7. Missing energy spectrum for the 153 MeV/c kinematics. (a) Before straight line background subtraction and showing the position of the line in red. (b) After straight line background subtraction.

in Fig. 5(b) where the simulation of the two-body breakup channel is represented in red.

D. Extraction of the cross section

The average cross section for the ^{4}He$(e, e'p)X$ reaction per missing momentum bin was extracted for the triton region and it is given by

$$\langle \sigma(p_m) \rangle = \frac{n(p_m) * \mathrm{RSC}}{\Delta\Omega_e \Delta\Omega_p \Delta E_e N_e N_{\mathrm{tgt}} * \mathrm{Eff}}, \tag{4}$$

where we have the following.

(a) $n(p_m)$ is the net counts in the triton region between missing energies of 0.017 and 0.022 GeV, after randoms and background subtraction. Since there is no model for the $X = 3N$ channels beyond 0.022 GeV, and since these channels reach 0.029 GeV, the background subtraction in the triton region was done using straight line subtraction below 0.029 GeV. An example of this background subtraction for 153 MeV/c kinematics is shown in Fig. 7. Figures 7(a) and 7(b) are before and after background subtraction, respectively. The net count in the triton region is obtained by the total counts in the shaded area in Fig. 7(b).

(b) RSC is the radiative and straggling corrections to the cross section due to the tail on the missing energy spectrum. These corrections are determined by comparing the number of events in a 5-MeV window centered on the triton peak to the total number of events in the GEANT simulation. There is little variation in RSC from the simulation between proton spectrometer settings: $1.33 < \mathrm{RSC} < 1.35$. There is an uncertainty of 0.2% in RSC.

(c) $\Delta\Omega_e$ and $\Delta\Omega_p$ are the geometrical solid angles of the spectrometer apertures.

(d) ΔE_e is the electron momentum bin in coincidence with protons. The choice of the bin size is determined by the proton arm by studying the dependency of the proton momentum versus the scattered electron momentum. A two-dimensional plot of proton momentum versus electron momentum for the total coincidence events is presented in Fig. 8 for the 153 MeV/c kinematics. Plots for higher momenta look similar with

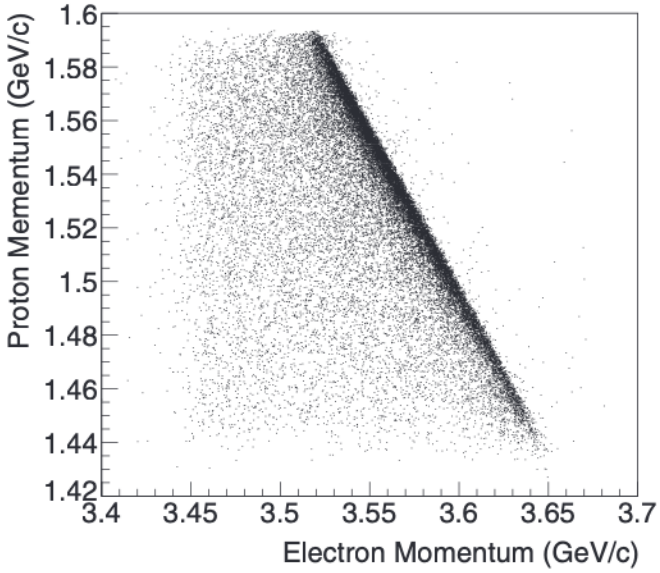

FIG. 8. Proton momentum versus electron momentum for the 153 MeV/c kinematics.

TABLE III. General uncertainties.

Efficiency	Value	Uncertainty (%)
Electronic live time	1	0
Trigger efficiency	0.97	1
Wire chamber efficiency	0.995	0.1
Tracking efficiency	0.9895	0.75

less statistics. This plot was then studied for various missing momentum bins for a given kinematics. This reduces the statistics, making the choice of ΔP somehow ambiguous. Therefore, a systematic uncertainty of 10% was attributed to ΔE_e.

(e) $N_e = Q/e$ is the number of electrons that passed through the target, where e is the electron charge and Q is the total charge. This is measured by the beam current monitors with an uncertainty of 0.3–0.5%.

(f) $N_{\text{tgt}} = \rho(I) * z_{\text{tgt}}$ is the number of nuclei per cm^2 in the beam. I is the beam current, $\rho(I)$ is the number of nuclei per cm^3, and z_{tgt} is the effective target length. Target densities along the ±8-cm effective target length for different beam currents are presented in Table II. N_{tgt} was known to 1.14%.

(g) Eff is the efficiency factor and it accounts for the following:
  (i) the missing momentum acceptance factor $f(p_m)$ that is explained in Sec. III B,
  (ii) data acquisition live time (LTdaq),
  (iii) electronics live time (LTel),
  (iv) trigger efficiency (Tri),
  (v) wire chamber (WC), and
  (vi) tracking efficiencies (Tra).
  This efficiency is given by

$$\text{Eff} = f(p_m) \cdot \text{LTd} \cdot \text{LTe} \cdot \text{Tri} \cdot \text{WC} \cdot \text{Tra}. \quad (5)$$

The live time of the trigger acquisition system, LTdaq, was 0.916 ± 0.01, and 0.95 ± 0.01 for the 153 MeV/c and 353 MeV/c kinematics, respectively. For the higher missing momentum settings, LTdaq was larger than 0.99, with negligible uncertainties. The remaining efficiencies are displayed in Table III.

To conclude this analysis section, a summary of the parameters involved in the cross-section calculations and their uncertainties are presented in the Appendix, Table IV. Experimental differential cross sections, $\frac{d\sigma^5}{d\Omega_p d\Omega_e dE_e}$, for ^{4}He$(e,e'p)X$, where $X = {}^3$H or $3N$, from E08009, for different kinematical settings given by the proton spectrometer central angle are presented in Table V. Statistical and normalization uncertainties are the first uncertainty entry; systematic uncertainties in selecting the size of the ΔE bin of 10% and an estimated 10% from the missing momentum acceptance factor, described in Sec. III B and Sec. III D, item (d), are the second uncertainty entry; and the total uncertainty is the third entry. The total uncertainly is calculated by adding statistical and normalization uncertainly and the systematic uncertainty in quadrature.

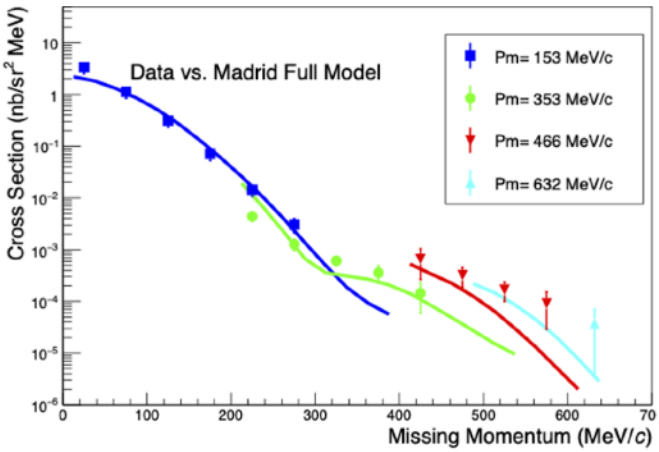

FIG. 9. E08009 data compared to Madrid full theoretical calculations. Blue squares are for the 153 MeV/c setting, green circles are for the 353 MeV/c setting, red inverted triangles are for the 466 MeV/c setting, and cyan triangles are for the 632 MeV/c setting. Theoretical calculations follow the same color code as the data for each momentum setting.

IV. RESULTS

A. Comparison of data to theoretical predictions

The extracted differential cross sections are compared to relativistic distorted-wave impulse approximation calculations of the Madrid theory group [15,21–23]. The ^{4}He ground state is described by a relativistic solution of the Dirac equation phenomenologically adjusted to fit the observed radius and binding energy of ^{4}He. These calculations were first introduced in Ref. [24].

Vertex values of the incident electron's momentum at various positions within the long gas target and the momenta of the scattered electron and the ejected proton were provided to the Madrid theory group for calculation of the cross section at each event vertex in the GEANT simulation. The GEANT simulation also contains the detected electron and proton momenta at the spectrometers' apertures. In this way the vertex cross section can be associated with the missing momentum at the apertures.

Theoretical cross sections integrated over the experimental acceptances for the full Madrid treatment and using the effective momentum approximation (EMA) treatment are presented in Tables VII and VIII. Plots of the data for the two theoretical treatments are shown in Figs. 9 and 10. For these kinematics, the EMA calculation is nearly indistinguishable from the full calculation, except for small differences at very low missing momentum.

Data and calculations show the same missing momenta dependence for the measured or calculated cross section as a function of kinematic setting. Even though the same magnitude of p_m is reached for different proton angles, the cross section does not simply factor as a function of p_m. Good agreements between the Madrid calculation and the data extend to about 420 MeV/c in missing momentum. It can be also noticed that both data and theory exhibit an inflection in the slope of the cross section between 300 and 400 MeV/c.

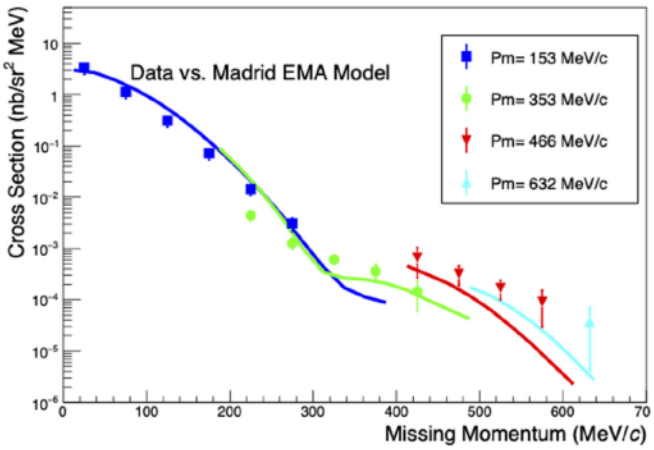

FIG. 10. E08009 data compared to Madrid EMA theoretical calculations. Blue squares are for the 153 MeV/c setting, green circles are for the 353 MeV/c setting, red inverted triangles are for the 466 MeV/c setting, and cyan triangles are for the 632 MeV/c setting. Theoretical calculations follow the same color code as the data for each momentum setting.

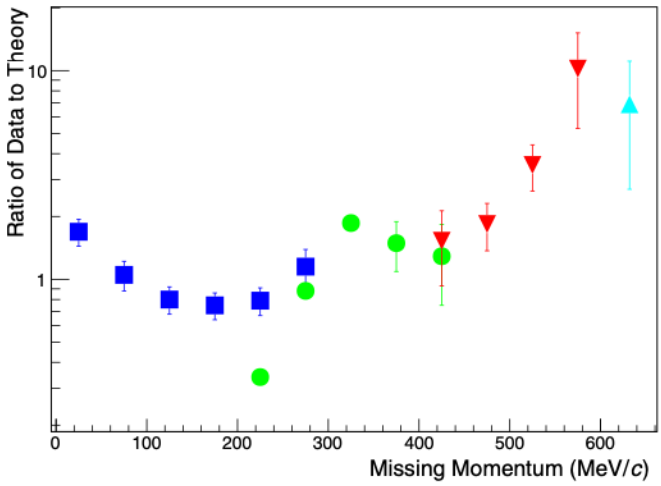

FIG. 11. Ratio of the experimental cross section to the theoretical Madrid full (pt) cross section versus missing momentum. Squares are for the 153 MeV/c setting, circles are for the 353 MeV/c setting, inverted triangles are for the 466 MeV/c setting, and triangles are for the 632 MeV/c setting.

In recent calculations on light nuclei [6], an inflection in the proton momentum distributions was predicted in the momentum range between 0.2 and 0.6 GeV/c. For ^{4}He, this inflection appears to be due to the triton + proton cluster distribution exhibiting a deep minimum in the proton momentum distribution. When added to the deuteron-deuteron cluster distribution, the inflection appears below and close to 0.4 GeV/c in the total proton density distribution, which is in agreement with the one we see in these data.

V. DISCUSSION AND CONCLUSION

For this experiment, the momenta of the outgoing proton and the scattered electron in the ^{4}He$(e, e'p)X$ reaction are measured. Using energy and momentum conservation, we can determine the momentum of the undetected hadronic state X. Theoretical comparison to the data here is limited to a specific exit channel, $X = {}^3$H. However, considering the theoretical cluster contributions to the proton momenta [6] in ^{4}He, the contribution of the pt cluster to the proton momentum distribution is expected to be negligible above about $p_m =$ 250 MeV/c.

The ratio of experimental cross section to the Madrid full predictions, in logarithmic scale, is shown in Fig. 11 for the four proton spectrometer central momentum settings. The blue squares, at the lowest missing momentum setting, hover around a ratio of 1, showing good agreement between data and predictions. The green dots are for the 0.353 GeV/c setting and we see a distinctive pattern for these data. The ratio at 0.225 GeV/c is 0.34, substantially different from the model prediction. This behavior cannot be traced to a statistical fluctuation because, as we see in Fig. 5(b), there is a substantial peak at the triton missing energy location. The cross section decreases by a factor of 12 between 0.225 and 0.325 GeV/c, and over the full range in missing momentum for this proton angle setting the cross section falls by a factor of 30. This fluctuation of the data to theory ratio suggests that some significant physics is not adequately included in the theoretical model for this range of missing momentum with these spectrometer settings. For the data at the 0.466 and 0.632 GeV/c settings, the ratio again shows a smooth missing momentum dependence.

However, the overall dependence of the cross section by the Madrid full model in Fig. 9 is qualitatively described.

From Ref. [6], the high proton momentum is attributed to the repulsive nucleon-nucleon core. Figure 5 shows a broad peak in the missing energy spectrum which shifts in position kinematically with the photon being absorbed on a correlated pair of nucleons. This feature has been previously seen in ^{3}He$(e, e'p)pn$ measurements in Refs. [11,25] and in the ^{4}He$(e, e'p)X$ continuum channel in Ref. [5].

The measurements of Korover *et al.* [7] are consistent with the NN short range force becoming repulsive. However, it is counterintuitive and in disagreement with theoretical expectations [6] that tritons should be ejected from ^{4}He along with protons emerging from short-range encounters.

The fact that we observe events in the triton region up to $p_m = 632$ MeV/c involves processes beyond the impulse approximation. Final-state interactions of the outgoing proton may take a proton knocked out of a pt cluster initially at a low value of p_p to appear as if its momentum at the vertex was p_m. This is accounted for to some extent by the optical model potential treatment of the final pt unbound state. We see good agreement between the theory and data in Fig. 9 up to about $p_m = 420$ MeV/c.

Beyond about 450 MeV/c in p_m substantially more triton region events are measured than what the Madrid full theory predicts. In this case three nucleons emitted at high p_m may be a signature of other reactions allowing the three-nucleon cluster to emerge as a bound or quasibound state. Since the kinematics for the electron were chosen for $x_b = 1.24$,

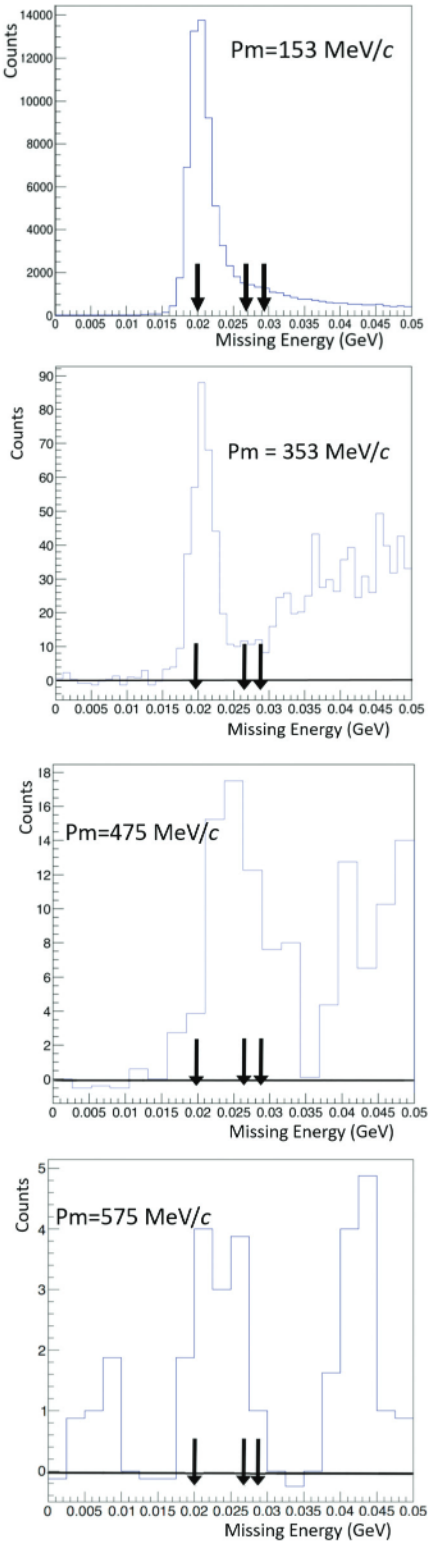

FIG. 12. From top to bottom: Missing energy region up to 50 MeV of excitation in ^{4}He$(e, e'p)X$ for $p_m = 153$, 352, 475, and 575 MeV/c, respectively. The three arrows point to the expected locations of the thresholds of the hadronic states $X = (t)$, $X = (n, d)$, and $X = (p, n, n)$.

protons in more intimate interactions with neighbors than quasielastic conditions ($x_b \approx 1$) may favor other reactions leading to three-nucleon clusters exiting in the missing energy region near the triton.

Portions of the missing energy spectrum in the triton/3N energy range are shown in Fig. 12. We see a change in the distribution of events as a function of missing momentum going from 153 to 575 MeV/c. At low missing momenta, the triton peak is centered at the expected value of 19.8 MeV. At higher missing momenta, the events are higher in missing energy by a few MeVs. From left to right, the three arrows in each figure point to the expected locations of the thresholds of the hadronic states $X = (t)$, $X = (n, d)$, and $X = (p, n, n)$, respectively.

An interesting question is the impact of three-nucleon forces, V_{ijk}, at high p_m. V_{ijk}'s are known to increase the binding energy of nuclei [3], so they would be natural actors in the formation of bound tritons or closely bound three-nucleon groups among the outgoing hadronic channels, X, at high missing momentum. The principal sources of data to help refine models of possible three-nucleon interactions are binding energies of ground and excited states of $A < 8$ nuclei and point proton charge distributions [3]. However, these data are not extensive enough to select unambiguously a particular set of parameters or models for V_{ijk}, and other observables are needed as discussed in Refs. [3,4].

More extensive and detailed data in the three-nucleon triton mass region and the existence of microscopic calculations for these nuclei open the possibility of exploiting the shapes of the missing energy spectra in $A(e, e'p)X$ reactions as additional observables for developing models of three-nucleon interactions.

ACKNOWLEDGMENTS

Special thanks to Silviu Covrig for providing the CFD calculations as a possibility to understanding the target vertex spectra for the SRC target. Special thanks to Or Hen for valuable discussions and inputs on the paper. The research presented in this paper is partially supported by the U.S. National Science Foundation under Grants No. PHY-2012413 (F.B.), No. PHY 16-15067 (F.B.), and No. PHY 09-69380 (K.A.). This work was supported by the U.S. Department of Energy under Contract No. DE-AC05-06OR23177 under which Jefferson Science Associates operates the Thomas Jefferson National Accelerator Facility.

APPENDIX: TABULATED RESULTS

Table IV summarizes the location of the parameters involved in the cross section in this document or their uncertainties. Experimental differential cross sections for ^{4}He$(e, e'p)X$, in nb/sr^2/MeV, are summarized in Table V for the four different spectrometer settings. Table VI summarizes the average values from the GEANT simulation of some kinematic variables in each of the 50-MeV-wide missing momentum bins used in the analysis. Tables VII and VIII summarize the Madrid full calculations and the Madrid EMA calculations, respectively, in the momentum range from 12.5 to 637.5 MeV/c.

TABLE IV. Parameters in the cross section calculation and their uncertainties.

Parameter	Location or values
RSC	Sec. III C and Sec. III D, item (b)
$\Delta\Omega_e$	4.8 msr ±2.7%, Fig. 4
$\Delta\Omega_p$	4.8 msr ±2.7%, Fig. 4
ΔE_e	Sec. III D, item (d), ±10%, Fig. 8
N_e	Sec. III D, item (e)
$N_{\rm tgt}$	Sec. III D, item (f), and Table II
Eff	Sec. III D, item (g)
$f(p_m)$	Eq. (3), discussed in Sec. III B, and Sec. III D, item (g.1)
LT(daq)	Sec. III D, item (g.2), depends on proton p_m setting
LT(el)	Sec. III D, item (g.3), and Table III
Tri	Sec. III D, item (g.4), and Table III
WC	Sec. III D, item (g.5), and Table III
Tra	Sec. III D, item (g.6), and Table III

TABLE V. Experimental differential cross sections, $\frac{d\sigma^5}{d\Omega_p d\Omega_e dE_e}$, for ^{4}He$(e,e'p)X$, where $X = {}^3$H or $3N$, from E08009, for different kinematical settings given by the proton spectrometer's central angle. Statistical and normalization uncertainties are the first uncertainty entry; systematic uncertainties in selecting the size of the ΔE bin of 10% and an estimated 10% from the missing momentum acceptance factor, described in Secs. III B and III D (d), are the second uncertainty entry; and the total uncertainty is the third entry. Units are nb/sr^2/MeV.

p_m (MeV/c)	153 $\theta_p = 47°$	353 $\theta_p = 38.5°$ $\times 10^{-4}$	466 $\theta_p = 33.5°$ $\times 10^{-4}$	632 $\theta_p = 29°$ $\times 10^{-5}$
25	$3.38 \pm 0.40 \pm 0.48 \pm 0.62$			
75	$1.13 \pm 0.13 \pm 0.16 \pm 0.20$			
125	$(3.13 \pm 0.36 \pm 0.44 \pm 0.57) \times 10^{-1}$			
175	$(7.18 \pm 0.83 \pm 1.02 \pm 1.31) \times 10^{-2}$			
225	$(1.44 \pm 0.17 \pm 0.20 \pm 0.26) \times 10^{-2}$	$44.0 \pm 1.4 \pm 6.2 \pm 6.4$		
275	$(3.06 \pm 0.48 \pm 0.43 \pm 0.65) \times 10^{-3}$	$12.7 \pm 1.3 \pm 1.8 \pm 2.2$		
325		$6.11 \pm 0.14 \pm 0.86 \pm 0.88$		
375		$3.57 \pm 0.80 \pm 0.50 \pm 0.95$		
425		$1.44 \pm 0.57 \pm \pm 0.20 \pm 0.61$	$(6.59 \pm 2.62 \pm 0.93 \pm 2.78)$	
475			$(3.22 \pm 0.83 \pm 0.46 \pm 0.95)$	
525			$(1.68 \pm 0.42 \pm 0.24 \pm 0.48)$	
575			$(0.91 \pm 0.42 \pm 0.13 \pm 0.44)$	
632				$(3.7 \pm 2.27 \pm 0.52 \pm 2.33)$

TABLE VI. Average values from the GEANT simulation of some kinematic variables in each of the 50-MeV-wide missing momentum bins used in the analysis. The bins are identified by the algebraic midpoints;for example, $p_m = 25$ is for the missing momentum bin from 0 to 50 MeV/c. The entries in each line are $\langle p_e \rangle$ in GeV/c, $\langle \theta_e \rangle$ in radians, $\langle \theta_p \rangle$ in radians, and $\langle p_m \rangle$ in MeV/c.

p_m (MeV/c)	$\overline{p_e}$ (GeV/c	$\overline{\theta_e}$ (rad)	$\overline{\theta_p}$ (rad)	$\overline{p_m}$ (rad)	$\overline{p_e}$ (GeV/c)	$\overline{\theta_e}$ (rad)	$\overline{\theta_p}$ (rad)	$\overline{p_m}$ (rad)	$\overline{p_e}$ (GeV/c)	$\overline{\theta_e}$ (rad)	$\overline{\theta_p}$ (rad)	$\overline{p_m}$ (rad)	$\overline{p_e}$ (GeV/c)	$\overline{\theta_e}$ (rad)	$\overline{\theta_p}$ (rad)	$\overline{p_m}$ (rad)
25	3.482	0.338	0.807	40.1												
75	3.495	0.345	0.817	81.0												
125	3.503	0.351	0.822	126.6												
175	3.527	0.353	0.822	175.2												
225	3.557	0.355	0.822	224.8	3.454	0.350	0.675	226.8								
275	3.591	0.356	0.821	274.3	3.488	0.353	0.673	275.6								
325					3.525	0.355	0.672	324.9								
375					3.565	0.355	0.672	374.8								
425					3.603	0.356	0.672	424.6	3.496	0.355	0.585	425.3				
475									3.542	0.355	0.585	474.9				
525									3.586	0.356	0.585	524.5				
575									3.619	0.359	0.584	573.8				
632													3.604	0.360	0.505	676.6

TABLE VII. Madrid full theoretical cross sections integrated over the experimental acceptances for ^{4}He$(e, e'p)^3$H for E08009, for different kinematical settings given by the proton spectrometer's central angle. Units are nb/sr^2/MeV.

p_m (MeV/c)	153 $\theta_p = 47°$	353 $\theta_p = 38.5°$	466 $\theta_p = 33.5°$	632 $\theta_p = 29°$
12.5	2.2059			
37.5	1.8287			
62.5	1.3139			
87.5	8.516×10^{-1}			
112.5	5.070×10^{-1}			
137.5	2.699×10^{-1}			
162.5	1.311×10^{-1}			
187.5	5.987×10^{-2}			
212.5	2.583×10^{-2}	1.918×10^{-2}		
237.5	1.044×10^{-2}	6.724×10^{-3}		
262.5	3.951×10^{-3}	2.209×10^{-3}		
287.5	1.370×10^{-3}	6.686×10^{-4}		
312.5	4.901×10^{-4}	3.578×10^{-4}		
337.5	1.858×10^{-4}	3.095×10^{-4}		
362.5	9.309×10^{-5}	2.687×10^{-4}		
387.5	5.639×10^{-5}	2.077×10^{-4}		
412.5		1.419×10^{-4}	5.283×10^{-4}	
437.5		8.366×10^{-5}	3.402×10^{-4}	
462.5		4.808×10^{-5}	2.225×10^{-4}	
487.5		2.739×10^{-5}	1.262×10^{-4}	2.206×10^{-4}
512.5		1.542×10^{-5}	6.542×10^{-5}	1.491×10^{-4}
537.5		9.478×10^{-6}	2.980×10^{-5}	8.585×10^{-5}
562.5			1.289×10^{-5}	4.400×10^{-5}
587.5			5.077×10^{-6}	1.977×10^{-5}
612.5			2.008×10^{-6}	7.741×10^{-6}
637.5			8.357×10^{-7}	2.834×10^{-6}

TABLE VIII. Madrid EMA theoretical cross sections integrated over the experimental acceptances for ^{4}He$(e, e'p)^3$H for E08009, for different kinematical settings given by the proton spectrometer's central angle. Units are nb/sr^2/MeV.

p_m (MeV/c)	153 $\theta_p = 47°$	353 $\theta_p = 38.5°$	466 $\theta_p = 33.5°$	632 $\theta_p = 29°$
37.5	2.681			
62.5	1.916			
87.5	1.235			
112.5	7.297×10^{-1}			
137.5	3.839×10^{-1}			
162.5	1.834×10^{-1}			
187.5	8.159×10^{-2}	9.031×10^{-2}		
212.5	3.382×10^{-2}	3.628×10^{-2}		
237.5	1.282×10^{-2}	1.295×10^{-2}		
262.5	4.433×10^{-3}	3.933×10^{-3}		
287.5	1.362×10^{-3}	9.986×10^{-4}		
312.5	4.312×10^{-4}	3.423×10^{-4}		
337.5	1.705×10^{-4}	2.643×10^{-4}		
362.5	1.130×10^{-4}	2.487×10^{-4}		
387.5	8.817×10^{-5}	2.083×10^{-4}		
412.5		1.547×10^{-4}	4.550×10^{-4}	
437.5		9.853×10^{-5}	3.082×10^{-4}	
462.5		6.482×10^{-5}	2.064×10^{-4}	
487.5		4.261×10^{-5}	1.206×10^{-4}	1.778×10^{-4}
512.5			6.435×10^{-5}	1.215×10^{-4}
537.5			3.036×10^{-5}	7.084×10^{-5}
562.5			1.360×10^{-5}	3.702×10^{-5}
587.5			5.527×10^{-6}	1.717×10^{-5}
612.5			2.251×10^{-6}	7.010×10^{-6}
637.5			9.483×10^{-7}	2.695×10^{-6}

[1] J. J. Kelly, Adv. Nucl. Phys. **23**, 75 (1996).
[2] M. M. Sargsian *et al.*, J. Phys. G: Nucl. Part. Phys. **29**, R1 (2003).
[3] S. C. Pieper, V. R. Pandharipande, R. B. Wiringa, and J. Carlson, Phys. Rev. C **64**, 014001 (2001).
[4] D. Lonardoni, A. Lovato, S. C. Pieper, and R. B. Wiringa, Phys. Rev. C **96**, 024326 (2017).
[5] J. M. Le Goff, M. Bernheim, M. K. Brussel, G. P. Capitani, J. F. Danel, E. De Sanctis, S. Frullani, F. Garibaldi, A. Gerard, M. Jodice, A. Magnon, C. Marchand, J. Morgenstern, J. Picard, D. Reffay, P. Vernin, and A. Zghiche, Phys. Rev. C **50**, 2278 (1994).
[6] R. B. Wiringa, R. Schiavilla, S. C. Pieper, and J. Carlson, Phys. Rev. C **89**, 024305 (2014).
[7] I. Korover *et al.*, Phys. Rev. Lett. **113**, 022501 (2014).
[8] R. Schiavilla, R. B. Wiringa, S. C. Pieper, and J. Carlson, Phys. Rev. Lett. **98**, 132501 (2007).
[9] M. M. Sargsian, T. V. Abrahamyan, M. I. Strikman, and L. L. Frankfurt, Phys. Rev. C **71**, 044615 (2005).
[10] M. Alvioli, C. Ciofi degli Atti, and H. Morita, Phys. Rev. Lett. **100**, 162503 (2008).
[11] F. Benmokhtar *et al.*, Phys. Rev. Lett. **94**, 082305 (2005).
[12] M. M. Rvachev *et al.*, Phys. Rev. Lett. **94**, 192302 (2005).
[13] W. U. Boeglin *et al.*, Phys. Rev. Lett. **107**, 262501 (2011).
[14] N. Liyanage *et al.*, Phys. Rev. Lett. **86**, 5670 (2001).
[15] J. M. Udias, J. R. Vignote, E. Moya de Guerra, A. Escuderos, and J. A. Caballero, arXiv:nucl-th/0109077.
[16] A. Aniol, F. Benmokhtar. S. Gilad, and D. Higinbotham, E08009 Experimental Proposal, https://www.jlab.org/exp_prog/CEBAF_EXP/E08009.html, Jefferson Laboratory, 2008.
[17] J. Alcorn *et al.*, Nucl. Instrum. Methods Phys. Res., Sect. A **522**, 294 (2004).
[18] S. Covrig (private communication).
[19] S. Iqbal, Thesis, California State University, Los Angeles, 2013, DOE/OR/23177-3086, https://misportal.jlab.org/ul/publications/view_pub.cfm?pub_id=13189.
[20] Instructions for COMGEANT, https://userweb.jlab.org/~gen/simul/, 2012 (unpublished).
[21] S. P. Malace *et al.*, Phys. Rev. Lett. **106**, 052501 (2011).
[22] R. Álvarez-Rodríguez *et al.*, Few-Body Syst. **50**, 359 (2011).
[23] J. M. Udias and J. R. Vignote, Phys. Rev. C **62**, 034302 (2000).
[24] M. Paolone *et al.*, Phys. Rev. Lett. **105**, 072001 (2010).
[25] C. Marchand, M. Bernheim, P. C. Dunn, A. Gérard, J. M. Laget, A. Magnon, J. Morgenstern, J. Mougey, J. Picard, D. Reffay-Pikeroen, S. Turck-Chieze, P. Vernin, M. K. Brussel, G. P. Capitani, E. De Sanctis, S. Frullani, and F. Garibaldi, Phys. Rev. Lett. **60**, 1703 (1988).